



OPEN

In situ IR spectroscopy during oxidation process of cobalt Prussian blue analogues

Hideharu Niwa^{1,2,3}✉, Toshiaki Moriya¹, Takayuki Shibata⁴, Yuya Fukuzumi¹ & Yutaka Moritomo^{1,2,3}✉

Cobalt Prussian blue analogues (Co-PBA; $\text{Na}_x\text{Co}[\text{Fe}(\text{CN})_6]_y$), consisting of cyano-bridged transition metal network, $-\text{Fe}-\text{CN}-\text{Co}-\text{NC}-\text{Fe}-$, are promising cathode materials for Na-ion secondary batteries. In the oxidation process, oxidation of Fe and/or Co are compensated by Na^+ deintercalation. Here, we investigated the oxidation process of three Co-PBAs by means of in situ infrared absorption (IR) spectroscopy. With use of an empirical rule of the frequencies of the CN^- stretching mode in ferrocyanide ($[\text{Fe}^{\text{II}}(\text{CN})_6]^{4-}$) and ferricyanide ($[\text{Fe}^{\text{III}}(\text{CN})_6]^{3-}$), the oxidation processes of Co-PBAs were determined against the Fe concentration (y) and temperature (T). We will discuss the interrelation between the oxidation processes and Fe concentration (y).

Prussian blue analogues (PBA; $A_xM[\text{Fe}(\text{CN})_6]_y$) consist of cyano-bridged three-dimensional transition metal network, $-M-\text{NC}-\text{Fe}-\text{CN}-M-\text{NC}-\text{Fe}-\text{CN}-M-$ (A and M are alkali and transition metals, respectively), and alkali cation located in the nanopores of the network. Among them, cobalt PBA (Co-PBA), represented as $\text{Na}_x\text{Co}[\text{Fe}(\text{CN})_6]_y$, have the face-centered cubic (fcc) ($Fm\bar{3}m$; $Z=4$) or trigonal ($R\bar{3}m$; $Z=3$) structures^{1–3}. The Co-PBA is one of the promising cathode materials for lithium-ion/sodium-ion secondary batteries^{4–14}, because Na^+ can be electrochemically intercalated into (deintercalated from) the nanopores of the network. The Na^+ deintercalation accompanies the oxidation of metal ions, *i.e.*, Fe and Co, from the divalent to trivalent states. As schematically shown in Fig. 1, PBA has two kinds of oxidation processes; $M^{\text{II}}\text{Fe}^{\text{II}} \rightarrow M^{\text{II}}\text{Fe}^{\text{III}} \rightarrow M^{\text{III}}\text{Fe}^{\text{III}}$ and $M^{\text{II}}\text{Fe}^{\text{II}} \rightarrow M^{\text{III}}\text{Fe}^{\text{II}} \rightarrow M^{\text{III}}\text{Fe}^{\text{III}}$, because it has two metal sites. We will call the former (latter) process as M^{II} -type (M^{III} -type) because M in the intermediate state is divalent (trivalent). The synchrotron-based X-ray absorption near edge structure (XANES) measurements and X-ray photoelectron spectroscopy (XPS) are powerful tool to determine the valence state of transition metals during the oxidization process^{8,15–21}. For example, Takachi et al. investigated the oxidization process of $\text{Na}_x\text{Mn}[\text{Fe}(\text{CN})_6]_{0.83}$ (NMF83) and $\text{Na}_x\text{Co}[\text{Fe}(\text{CN})_6]_{0.90}$ (NCF90), and found that the processes are classified into M^{II} -type and M^{III} -type, respectively⁸.

On the other hands, infrared (IR) spectroscopy is a sensitive probe of the CN^- stretching mode. Especially, the spectroscopy can clarify the effect of the valence changes of the sandwiching M and Fe, *i.e.*, $M-\text{NC}-\text{Fe}$, on the CN^- stretching mode. Several researchers^{6,22–31} have reported the characteristic valence effect on the mode. In Table 1, we summarized the interrelation between the frequency (ν_{CN}) of the CN^- stretching mode and the valence of the neighboring Fe, that is, divalent in ferrocyanide ($[\text{Fe}^{\text{II}}(\text{CN})_6]^{4-}$) and trivalent ferricyanide ($[\text{Fe}^{\text{III}}(\text{CN})_6]^{3-}$). Regardless of A and M , the ν_{CN} in ferrocyanide (ferricyanide) is ranged from 2065 to 2135 cm^{-1} (2145 to 2205 cm^{-1}). Hereafter, we will call this relation as “empirical rule”. The empirical rule tells us that Fe takes divalent (trivalent) if $\nu_{\text{CN}} < 2135 \text{ cm}^{-1}$ ($\nu_{\text{CN}} > 2145 \text{ cm}^{-1}$). On the other hands, Moriya et al. performed in situ IR spectroscopy of Co- and Mn-PBAs³². They clarified the persistent and/or amalgamation type behavior of the CN^- stretching mode during the oxidization process. The persistent and/or amalgamation type behavior are well classified by magnitude of Δ/W , where Δ and W are the energy difference between divalent and trivalent states and band width of the CN^- stretching mode, respectively. Thus, IR spectroscopy is a sensitive probe for the CN^- stretching mode. And, there exists the empirical rule between the Fe valence and ν_{CN} . Then, we can detect the valence change of Fe and M via ν_{CN} during the oxidization process, and hence, can determine the type of the oxidization process, *i.e.* M^{II} and M^{III} -type.

¹Graduate School of Pure and Applied Sciences, University of Tsukuba, Tsukuba 305-8571, Japan. ²Faculty of Pure and Applied Sciences, University of Tsukuba, Tsukuba 305-8571, Japan. ³Tsukuba Research Center for Energy Materials Science (TREMS), University of Tsukuba, Tsukuba 305-8571, Japan. ⁴National Institute of Technology, Gunma College, Maebashi, Gunma 371-8530, Japan. ✉email: niwa.hideharu.ga@u.tsukuba.ac.jp; moritomo.yutaka.gf@u.tsukuba.ac.jp

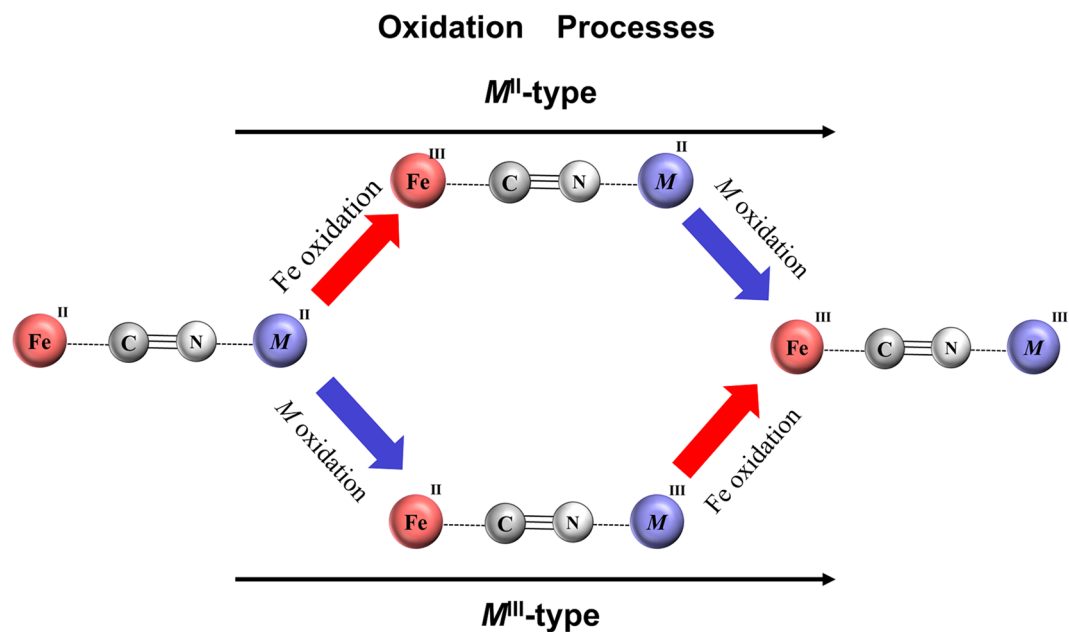


Figure 1. Oxidation processes in $A_xM[Fe(CN)_6]_y$. We call the upper and lower processes as M^{II} -type and M^{III} -type, respectively.

<i>M</i>	<i>A</i>	Fe^{II}		Fe^{III}		References
		Samples	ν_{CN} (cm^{-1})	Samples	ν_{CN} (cm^{-1})	
Co	–	$Co_2[Fe(CN)_6]$	2085	$Co_3[Fe(CN)_6]_2$	2160, 2200	22
Co	Na	$Na_{1.4}Co_{1.3}[Fe(CN)_6]$	2100	$Na_{0.4}Co_{1.3}[Fe(CN)_6]$	2160	23
Co	K	$K_{0.4}Co_{1.3}[Fe(CN)_6]$	2135			23
Co	Na	$Na_{0.84}Co[Fe(CN)_6]_{0.71}$	2080	$Na_{0.23}Co[Fe(CN)_6]_{0.71}$	2160	24
Co	K	$K_{0.1}Co_4[Fe(CN)_6]_{2.7}$	2090, 2118	$K_{0.1}Co_4[Fe(CN)_6]_{2.7}$	2156	25
	Rb	$Rb_{1.8}Co_4[Fe(CN)_6]_{3.3}$	2125			
	Cs	$Cs_{3.9}Co_4[Fe(CN)_6]_{3.9}$	2120			
Co	–	$Co_2[Fe(CN)_6]$	2080	$Co_3[Fe(CN)_6]_2$	2156	26
	–			$Co[Fe(CN)_6]$	2190–2205	
Co	–	$Co_3[Fe(CN)_6]_2$	2080, 2120	$Co_3[Fe(CN)_6]_2$	2160	27
Co	Rb	$Rb_{0.4}Co_4[Fe(CN)_6]_{2.8}$	2095	$Rb_{0.4}Co_4[Fe(CN)_6]_{2.8}$	2159	28
Co	–	$Co_3[Fe(CN)_6]_2$	2091, 2117	$Co_3[Fe(CN)_6]_2$	2158	29
Co	K	$K_2Co[Fe(CN)_6]$	2087	$Co_3[Fe(CN)_6]_2$	2155	30
	K	$K_2Co_3[Fe(CN)_6]$	2105	$Co[Fe(CN)_6]$	2200	
	K	$K_{0.4}Co_{1.3}[Fe(CN)_6]$	2113–2130			
Mn	–	$Mn_3[Fe(CN)_6]_2$	2066	$Mn_3[Fe(CN)_6]_2$	2147	29
Mn	Na	$Na_{1.32}Mn[Fe(CN)_6]_{0.83}$	2070	$Mn[Fe(CN)_6]_{0.83}$	2150	8
Mn	–	$Mn_3[Fe(CN)_6]_2$	2070	$Mn_3[Fe(CN)_6]_2$	2149	31

Table 1. The frequency (ν_{CN}) of the CN^- stretching mode in $[Fe^{II}(CN)_6]^{4-}$ and $[Fe^{III}(CN)_6]^{3-}$ in Prussian blue analogues (PBA; $A_xM[Fe(CN)_6]_y$).

In this paper, we will demonstrate that the in situ IR spectroscopy is a sensitive tool to determine the type of the oxidation process. We investigated the oxidation process of three Co-PBAs with different Fe concentration ($y=0.71, 0.81, \text{ and } 0.90$) and temperature ($T=293$ and 330 K). With use of the empirical rule of the CN^- stretching mode, the oxidation processes of Co-PBA were classified into the M^{II} -type or M^{III} -type without ambiguity.

Results

Figure 2a shows in situ IR spectra of the NCF90 film measured at 293 K. The horizontal arrows indicate the empirical region for the CN^- stretching modes in ferrocyanide ($[Fe^{II}(CN)_6]^{4-}$) and ferricyanide ($[Fe^{III}(CN)_6]^{3-}$), respectively. Figure 2b shows the corresponding charge curve of the NCF90 film against x at 1.6 C. The charge curve shows two plateaus at around 3.5 and 4.0 V vs. Na/Na^+ , indicating two step oxidation process. In the

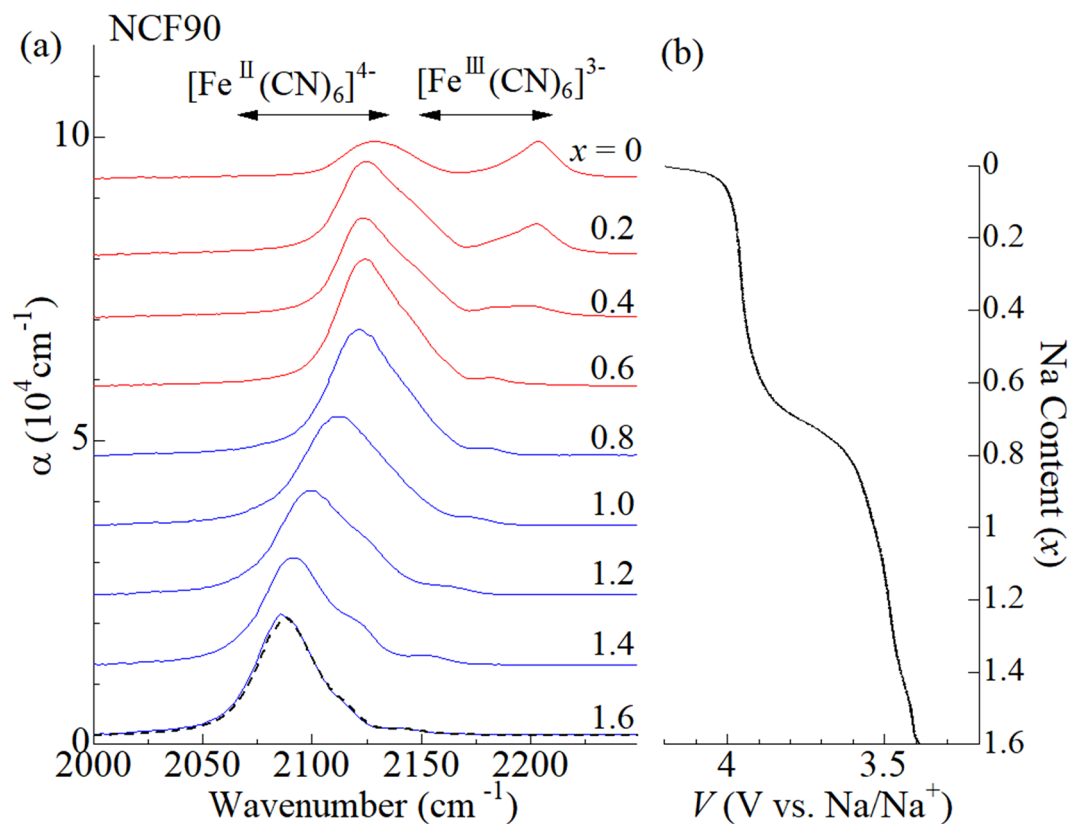


Figure 2. (a) In situ IR spectra of the NCF90 film at 293 K against Na concentration (x) in the oxidation process from $x = 1.6$ to $x = 0$. Black broken curve at $x = 1.6$ was obtained after the measurement. α is absorption coefficient; $\alpha = \frac{1}{d} \ln \frac{I_0}{I}$, where d is the film thickness, I_0 is the incident beam intensity, and I is the transmitted beam intensity, respectively. Spectra are vertically shifted for clarity. The horizontal arrows indicate the empirical region for the CN^- stretching modes in $[\text{Fe}^{\text{II}}(\text{CN})_6]^{4-}$ and $[\text{Fe}^{\text{III}}(\text{CN})_6]^{3-}$, respectively. (b) Charge curve of NCF90 film at 293 K against x at 1.6 C. The voltages of the electrochemical cell were scaled to vs. Na/Na^+ .

lower-lying plateau near 3.5 V, single CN^- stretching mode is observed in the range from 2080 cm^{-1} to 2120 cm^{-1} . The empirical rule of the CN^- stretching mode (horizontal arrows) indicates that the Fe remains divalent in this plateau. Then, the oxidation process in the lower-lying plateau is carried out by the valence change of Co from Co^{2+} to Co^{3+} . Reflecting the valence change of Co, the CN^- stretching mode shows blue shift with decrease in x . In the higher-lying plateau, an additional CN^- stretching mode appears at around 2200 cm^{-1} . The spectral weight transfers from lower-lying band at 2120 cm^{-1} to the higher-lying band at 2200 cm^{-1} with decrease in x . The empirical rule of the CN^- stretching mode indicates that the additional mode at 2200 cm^{-1} is due to ferricyanide. In short, the redox site in the higher-lying plateau is Fe, because the divalent and trivalent Fe coexist. Thus, the in situ IR spectroscopy classifies the oxidation process of NCF90 into the M^{III} -type. The classification is consistent with the literature^{8,15}.

Figure 3a shows in situ IR spectra of $\text{Na}_{0.84}\text{Co}[\text{Fe}(\text{CN})_6]_{0.71}$ (NCF71) film measured at 293 K. The horizontal arrows indicate the empirical region for the CN^- stretching modes in ferrocyanide ($[\text{Fe}^{\text{II}}(\text{CN})_6]^{4-}$) and ferricyanide ($[\text{Fe}^{\text{III}}(\text{CN})_6]^{3-}$), respectively. Figure 3b shows the corresponding charge curve of the NCF71 film against x at 1.9 C. The charge curve shows two plateaus at around 3.5 and 4.0 V vs. Na/Na^+ , indicating two step oxidation process. In the lower-lying plateau, two CN^- stretching modes are observed in the range at around 2090 cm^{-1} and 2155 cm^{-1} . The spectral weight transfers from lower-lying band at 2090 cm^{-1} to the higher-lying band at 2155 cm^{-1} with decrease in x . The empirical rule indicates that the former and latter mode are ascribed to the ferrocyanide and ferricyanide, respectively. In short, the redox site in the lower-lying plateau is Fe, because the divalent and trivalent Fe coexist. In the higher-lying plateau, two CN^- stretching modes are observed in the range at around 2155 cm^{-1} and 2185 cm^{-1} . The empirical rule indicates that the Fe is trivalent in this plateau. Then, the oxidation process in the higher-lying plateau is carried out by the valence change of Co from Co^{2+} to Co^{3+} . With decrease in x , the spectral weight transfers from the lower-lying to higher-lying bands. Therefore, the lower-lying (higher-lying) band can be ascribed to the $\text{Fe}^{\text{III}}\text{-CN-Co}^{\text{II}}$ ($\text{Fe}^{\text{III}}\text{-CN-Co}^{\text{III}}$) mode. Thus, the in situ IR spectroscopy classifies the oxidation process of NCF71 into the M^{II} -type. The classification is consistent with the literature²³.

Figure 4a shows in situ IR spectra of the $\text{Na}_{1.24}\text{Co}[\text{Fe}(\text{CN})_6]_{0.81}$ (NCF81) film measured at 293 K. Figure 4b shows the corresponding charge curve of the NCF81 film against x at 2.0 C. The charge curve shows two plateaus at around 3.5 and 3.8 V vs. Na/Na^+ , indicating two step oxidation process. In the lower-lying plateau near 3.5 V, single CN^- stretching mode is observed in the range from 2085 cm^{-1} to 2125 cm^{-1} . The empirical rule indicates that the Fe is divalent in this plateau. Then, the oxidation process in the lower-lying plateau is carried out by

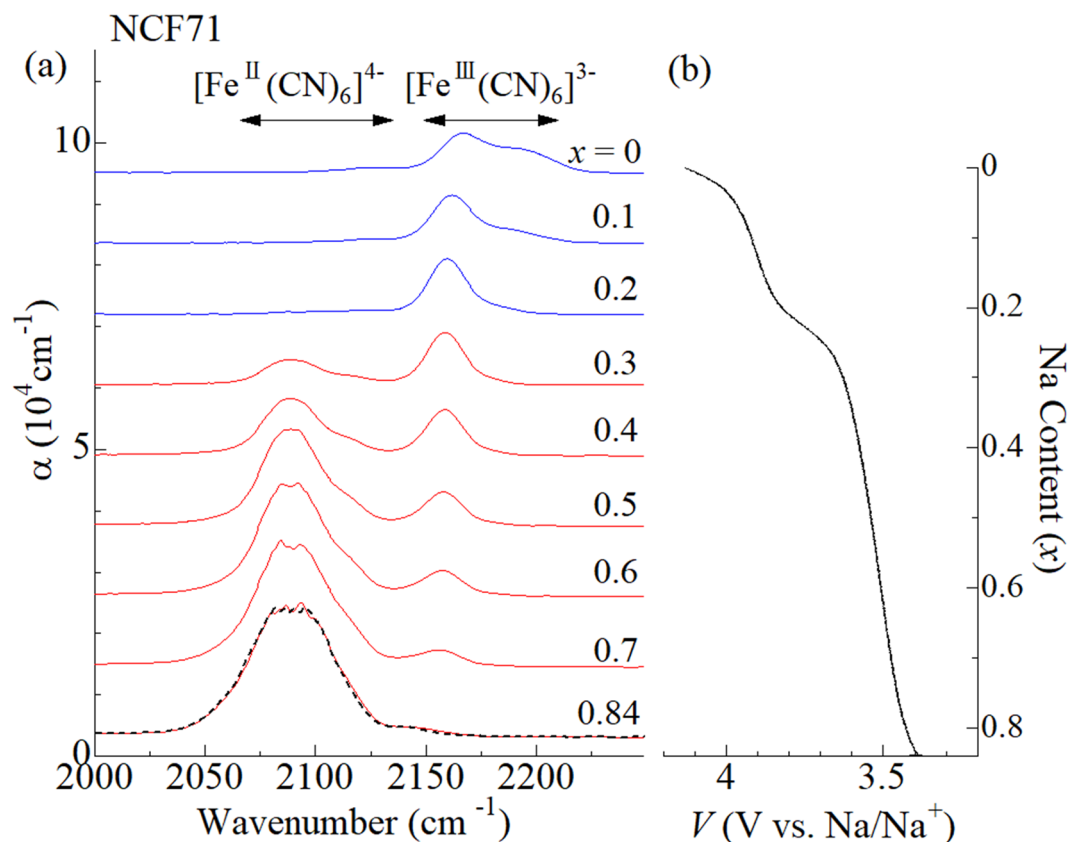


Figure 3. (a) In situ IR spectra of the NCF71 film at 293 K against x in the oxidation process from $x=0.84$ to $x=0$. Black broken curve at $x=0.84$ was obtained after the measurement. α is absorption coefficient; $\alpha = \frac{1}{d} \ln \frac{I_0}{I}$, where d is the film thickness, I_0 is the incident beam intensity, and I is the transmitted beam intensity, respectively. Spectra are vertically shifted for clarity. The horizontal arrows indicate the empirical region for the CN^- stretching modes in $[\text{Fe}^{\text{II}}(\text{CN})_6]^{4-}$ and $[\text{Fe}^{\text{III}}(\text{CN})_6]^{3-}$, respectively. (b) Charge curve of the NCF71 film at 293 K against x at 1.9 C. The voltages of the electrochemical cell were scaled to vs. Na/Na^+ .

the valence change of Co from Co^{2+} to Co^{3+} . Reflecting the valence change of Co, the CN^- stretching mode shows blue shift with decrease in x . In the higher-lying plateau, an additional CN^- stretching mode appears at around 2200 cm^{-1} . The spectral weight transfers from lower-lying band at 2125 cm^{-1} to the higher-lying band at 2200 cm^{-1} with decrease in x . The empirical rule indicates that the additional mode at 2200 cm^{-1} is due to ferricyanide. In short, the redox site in the higher-lying plateau is Fe, because the divalent and trivalent Fe coexists. Thus, the in situ IR spectroscopy classifies the oxidation process of NCF81 at 293 K into the M^{III} -type.

Figure 5a shows in situ IR spectra of the NCF81 film at 330 K. We note that the x -dependent spectral changes of the NCF81 film are qualitatively different between at 293 K (Fig. 4a) and at 330 K (Fig. 5a). Figure 5b shows the corresponding charge curve of the NCF81 film at 1.4 C. The charge curve shows two plateaus at around 3.6 and 3.8 V vs. Na/Na^+ , indicating two step oxidation process. In the lower-lying plateau near 3.6 V, two CN^- stretching modes are observed in the range at around 2090 cm^{-1} and 2155 cm^{-1} . The spectral weight transfers from lower-lying band at 2090 cm^{-1} to the higher-lying band at 2155 cm^{-1} with decrease in x . The empirical rule indicates that the former and latter mode are ascribed to the ferrocyanide and ferricyanide, respectively. In short, the redox site in the lower-lying plateau is Fe, because the divalent and trivalent Fe coexists. In the higher-lying plateau near 3.8 V, two CN^- stretching modes are observed in the range at around 2155 cm^{-1} and 2195 cm^{-1} . The empirical rule indicates that the Fe is trivalent in this plateau. Then, the oxidation process in the higher-lying plateau is carried out by the valence change of Co from Co^{2+} to Co^{3+} . With decrease in x , the spectral weight transfers from the lower-lying to higher-lying band. Therefore, the lower-lying (higher-lying) band can be ascribed to the $\text{Fe}^{\text{III}}\text{-CN-Co}^{\text{II}}$ ($\text{Fe}^{\text{III}}\text{-CN-Co}^{\text{III}}$) mode. Thus, the in situ IR spectroscopy classifies the oxidation process of NCF81 at 330 K into the M^{II} -type.

Discussion

We investigated the redox process of four (y, T) points, i.e., $(0.71, 293 \text{ K})$, $(0.81, 293 \text{ K})$, $(0.90, 293 \text{ K})$, and $(0.81, 330 \text{ K})$, where y is the Fe concentration. The IR spectroscopy revealed that $(y, T) = (0.71, 293 \text{ K})$ and $(0.81, 330 \text{ K})$ points are M^{II} -type, and $(y, T) = (0.81, 293 \text{ K})$ and $(0.90, 293 \text{ K})$ points are M^{III} -type. In the y - T plane, the M^{II} -type reaction appears when the T is raised or y is lowered from the $(0.81, 293 \text{ K})$ point.

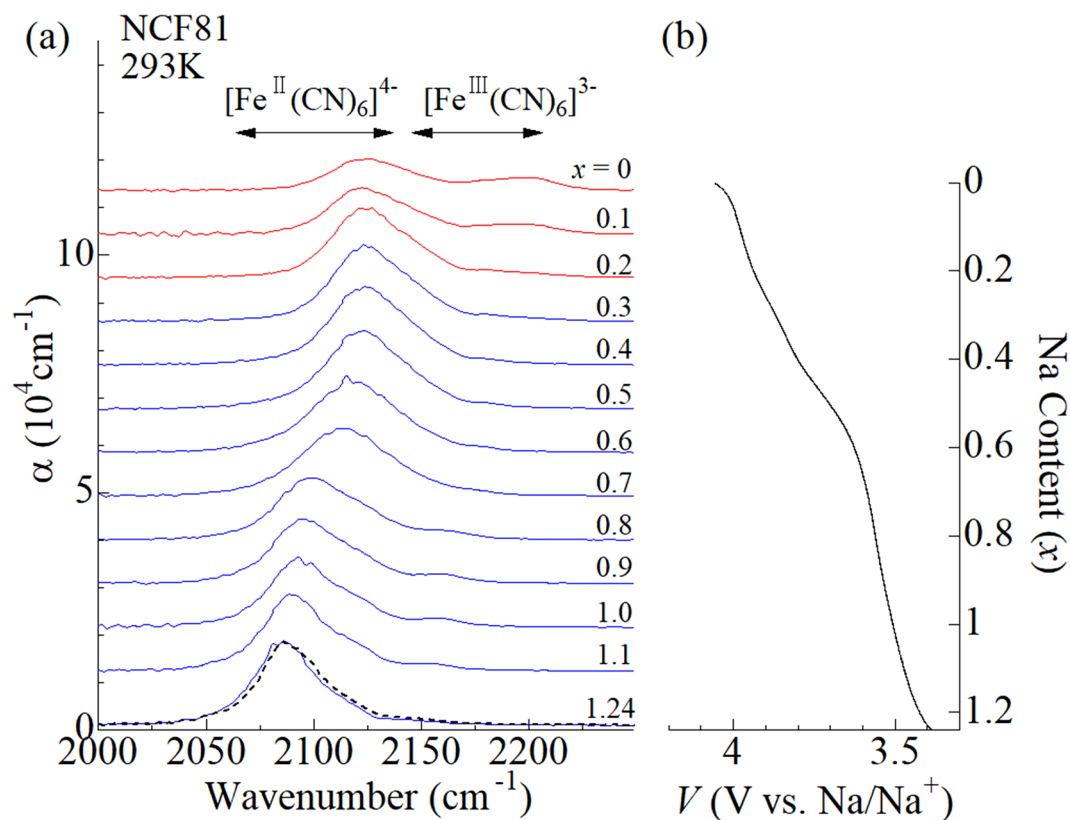


Figure 4. (a) In situ IR spectra of the NCF81 film at 293 K against x in the oxidation process from $x=1.24$ to $x=0$. Black broken curve at $x=1.24$ was obtained after the measurement. α is absorption coefficient; $\alpha = \frac{1}{d} \ln \frac{I_0}{I}$, where d is the film thickness, I_0 is the incident beam intensity, and I is the transmitted beam intensity, respectively. Spectra are vertically shifted for clarity. The horizontal arrows indicate the empirical region for the CN^- stretching modes in $[\text{Fe}^{\text{II}}(\text{CN})_6]^{4-}$ and $[\text{Fe}^{\text{III}}(\text{CN})_6]^{3-}$, respectively. (b) Charge curve of the NCF81 film measured at 293 K against x at 2.0 C. The voltages of the electrochemical cell were scaled to vs. Na/Na^+ .

The Co-PBA in the intermediate state shows a phase transition from low-spin (LS) to high-spin (HS) phases with increase in temperature^{33,34}. The electronic configuration is LS Co^{3+} and LS Fe^{2+} in the LS phase, while it is HS Co^{2+} and LS Fe^{3+} in the HS phase. The phase transition accompanies cooperative charge transfer from Fe^{2+} to Co^{3+} as well as the expansion of the unit cell volume. The volume expansion is ascribed to the larger ionic radius of HS Co^{2+} . We consider that the relative stability of the two phases in the intermediate state determines the type of the oxidation process; the oxidation process is M^{III} -type if the LS phase is stable, while the oxidation process is M^{II} -type if the HS phase is stable. The HS state, and hence, the M^{II} -type process, is stabilized with decrease in y , because the weaker ligand field from the octahedrally coordinated $[\text{Fe}(\text{CN})_6]$ stabilizes the HS Co^{2+} configuration. This argument well explains why the M^{II} -type reaction appears when the T is raised, or y is lowered.

Summary

We demonstrated that the in situ IR spectroscopy is a sensitive tool to determine the type of the oxidation process. The oxidation processes were classified into the M^{II} -type or M^{III} -type against Fe concentration (y) and temperature; The $y=0.71$ (at 293 K) and 0.81 (at 330 K) compounds are classified into M^{II} -type while the $y=0.81$ (at 293 K) and 0.90 (at 293 K) compounds are classified into M^{III} -type. Especially, the $y=0.81$ shows thermal switching of the oxidation process from the M^{III} -type (293 K) to M^{II} -type (at 330 K). Such a thermal switching is advantageous for thermal energy harvesting, as demonstrated by Shibata et al.³⁵ in the tertiary battery with use of phase transition.

Methods

Sample preparation. Thin films of $\text{Na}_{1.60}\text{Co}[\text{Fe}(\text{CN})_6]_{0.9}$ (NCF90), $\text{Na}_{1.24}\text{Co}[\text{Fe}(\text{CN})_6]_{0.81}$ (NCF81), $\text{Na}_{0.84}\text{Co}[\text{Fe}(\text{CN})_6]_{0.71}$ (NCF71), and $\text{Na}_{0.72}\text{Ni}[\text{Fe}(\text{CN})_6]_{0.68}$ (NNF68) were synthesized by electrochemical decomposition method. The films were deposited on the indium tin oxide (ITO) transparent electrode coated on cover glass substrate under potentiostatic conditions at -0.45 V vs. the Ag/AgCl electrode. The electrolytes for the NCF90 film³⁶ were an aqueous solution containing 0.8 mmol/L $\text{K}_3[\text{Fe}(\text{CN})_6]$, 0.5 mmol/L $\text{Co}(\text{NO}_3)_2$, and 5.0 mol/L NaNO_3 . The electrolytes for the NCF81 film³⁵ were an aqueous solution containing 0.8 mmol/L $\text{K}_3[\text{Fe}(\text{CN})_6]$, 0.5 mmol/L $\text{Co}(\text{NO}_3)_2$, and 0.5 mol/L NaNO_3 . The electrolytes for the NCF71 film²⁴ were an aqueous solution containing 0.5 mmol/L $\text{K}_3[\text{Fe}(\text{CN})_6]$, 1.25 mmol/L $\text{Co}(\text{NO}_3)_2$, and 1.0 mol/L NaNO_3 . The electro-

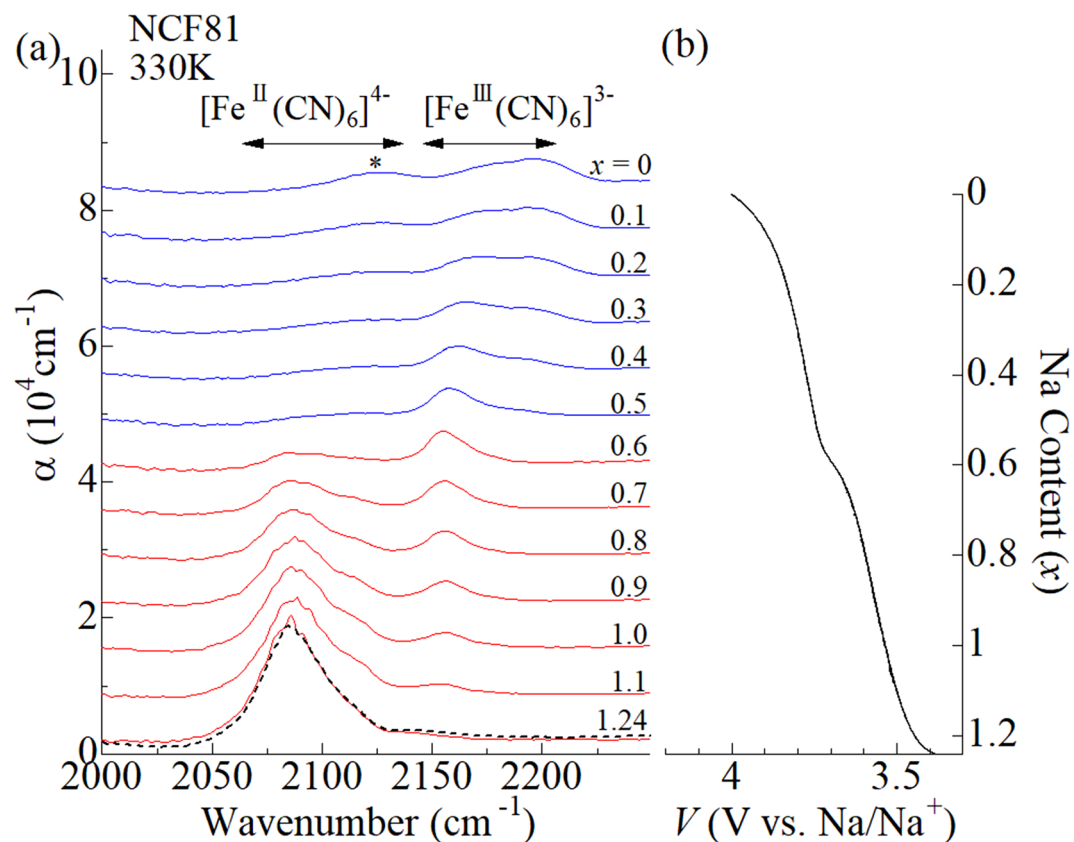


Figure 5. (a) In situ IR spectra of the NCF81 film at 330 K against x in the oxidation process from $x = 1.24$ to $x = 0$. Black broken curve at $x = 1.24$ was obtained after the measurement. α is absorption coefficient; $\alpha = \frac{1}{d} \ln \frac{I_0}{I}$, where d is the film thickness, I_0 is the incident beam intensity, and I is the transmitted beam intensity, respectively. Spectra are vertically shifted for clarity. The horizontal arrows indicate the empirical region for the CN stretching modes in $[\text{Fe}^{\text{II}}(\text{CN})_6]^{4-}$ and $[\text{Fe}^{\text{III}}(\text{CN})_6]^{3-}$, respectively. Origin of the band marked by asterisk is unknown. (b) Charge curve of the NCF81 film at 330 K against x at 1.4 C. The voltages of the electrochemical cell were scaled to vs. Na/Na⁺.

Samples	Electrolytes	Concentrations	Deposition time
NCF90	$\text{K}_3[\text{Fe}(\text{CN})_6]$	0.8 mmol/L	30 min
	$\text{Co}(\text{NO}_3)_2$	0.5 mmol/L	
	NaNO_3	5.0 mol/L	
NCF81	$\text{K}_3[\text{Fe}(\text{CN})_6]$	0.8 mmol/L	15 min
	$\text{Co}(\text{NO}_3)_2$	0.5 mmol/L	
	NaNO_3	0.5 mol/L	
NCF71	$\text{K}_3[\text{Fe}(\text{CN})_6]$	0.5 mmol/L	15 min
	$\text{Co}(\text{NO}_3)_2$	1.25 mmol/L	
	NaNO_3	1.0 mol/L	
NNF68	$\text{K}_3[\text{Fe}(\text{CN})_6]$	0.5 mmol/L	45 min
	$\text{Ni}(\text{NO}_3)_2$	0.5 mmol/L	
	NaNO_3	1.0 mol/L	

Table 2. Synthesis condition of PBA films by electrochemical decomposition method.

lytes for the NNF68 film were an aqueous solution containing 0.5 mmol/L $\text{K}_3[\text{Fe}(\text{CN})_6]$, 0.5 mmol/L $\text{Ni}(\text{NO}_3)_2$, and 1.0 mol/L NaNO_3 . Synthesis condition of the PBA films are summarized in Table 2. In this process, the reduction reaction ($[\text{Fe}(\text{CN})_6]^{3-} + e^- \rightarrow [\text{Fe}(\text{CN})_6]^{4-}$) triggers the deposition of PBAs. Therefore, Fe, Co and Ni in the as-grown films are divalent. Among the three Co-PBA film, NCF90 film shows the highest discharge capacity (135 mAh/g)⁸. In addition, the NCF90 film exhibits excellent rate properties (discharge capacity at 60C is 90% of the OCV value)⁸.

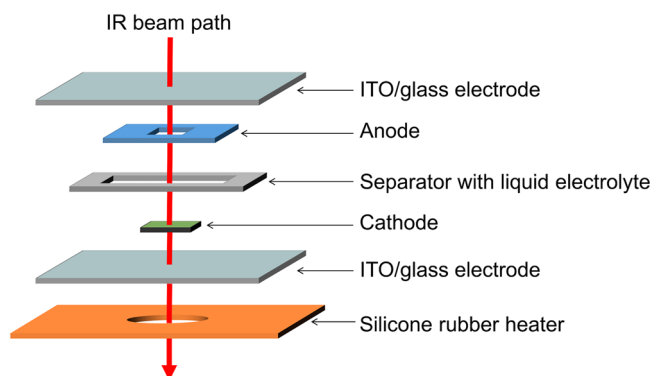


Figure 6. Schematic representation of the optical electrochemical cell for in situ IR measurements.

The X-ray diffraction patterns of the NNF68, NCF71, NCF81, and NCF90 films at 293 K were shown in Figure S1. The X-ray source was the Cu K α line. NNF68, NCF71, and NCF81 show face-centered cubic (fcc) ($Fm\bar{3}m$; $Z=4$) structure. The lattice constants (a) of NNF68, NCF71, and NCF81 are 10.15 Å, 10.26 Å, and 10.26 Å, respectively. NCF90 shows trigonal ($R\bar{3}m$; $Z=3$) structure. The lattice constants a and c of NCF90 are 7.40 Å and 17.49 Å. The chemical compositions of the films were determined by the inductively coupled plasma (ICP) method and CHN organic elementary analysis (PerkinElmer 2400 CHN Elemental Analyzer). Thickness of the NCF90, NCF81, and NCF71 films were 1.36 μm , 1.39 μm , and 1.93 μm , respectively, which were evaluated by a profilometer (aep Technology NanoMap-LS).

In situ infrared spectroscopy. The in situ IR spectra were measured with the use of an infrared microscopy system (JASCO IRT-3000) equipped with a Fourier transform infrared spectrometer (JASCO FT/IR-660 Plus) in the 400–7000 cm^{-1} region with 2 cm^{-1} resolution. The transmitted light was focused on a cooled HgCdTe detector. The Na concentrations (x) were electrochemically controlled in the oxidation (charging) process with a potentiostat (Bio-logic VSP multichannel potentiostat). x in NCF90, NCF81, and NCF71 films were evaluated from the extracted charge under the assumption that $x=0.0$ in the fully oxidized state. In situ IR spectra of NCF71, NCF81, and NCF90 at 293 K were measured in the first oxidation process films. The spectra of NCF81 at 330 K were measured in the second oxidation process films after the measurement at 293 K. We confirmed that the spectral profiles returned to the initial ones after the reduction process. Each spectrum was recorded in every 90 s during the oxidization process.

Optical electrochemical cell. Figure 6 schematically shows the optical electrochemical cell used for the in situ IR measurements. The cathode, anode and electrolyte were the Co-PBA and NNF68 film grown on the ITO glass substrates, and 17 mol/kg NaClO₄ aqueous solution. To measure the IR spectra of the Co-PBA film, the center of NNF68 film has hollow. The anode and cathode sandwich a separator whose thickness was 25 μm . The voltage between the anode and cathode was controlled so that a constant current (75 $\mu\text{A}/\text{cm}^2$) would flow between the electrodes. The voltage control range was from -0.05 V to 1.0 V vs. NNF68. The cell temperature was controlled by a silicone rubber heater. IR absorptions due to the ITO glass substrates and the electrolyte were subtracted as backgrounds.

We chose the NNF68 film as anode, because the film is stable in aqueous electrolyte³⁷. The anode NNF68 were pre-oxidized to 3.45 V vs. Na/Na⁺. The active area of anode (213 mm^2) was set to be much larger than that of cathode (4 mm^2) so that x , and hence, the potential of anode can be regarded as constant, as schematically shown in Fig. S2. Therefore, the voltage vs. Na/Na⁺ can be obtained by adding 3.45 V to the voltage vs. NNF68 in the optical cell. In the in situ IR experiment, the current density was determined so that the charge rate was 1 C (= 75 $\mu\text{A}/\text{cm}^2$), assuming that the film thickness was 1 μm . After the measurement, the film thickness was determined with use of the profilometer. Mass was evacuated from the thickness and area (= 4 mm^2). Mass of the NCF90, NCF81, and NCF71 films were 5.8 μg , 6.6 μg , and 6.7 μg , respectively. The actual charge rate of NCF90 at 293 K, NCF81 at 293 K, NCF81 at 330 K, and NCF71 at 293 K were 1.6 C, 2.0 C, 1.4 C, and 1.9 C, respectively.

Received: 13 November 2020; Accepted: 5 February 2021

Published online: 18 February 2021

References

- Moritomo, Y., Matsuda, T., Kurihara, Y. & Kim, J. Cubic-rhombohedral structural phase transition in Na_{1.32}Mn[Fe(CN)₆]_{0.83}·3.6H₂O. *J. Phys. Soc. Japan* **80**, 074608 (2011).
- Moritomo, Y., Matsuda, T., Kurihara, Y. & Kim, J. Erratum: “Cubic-rhombohedral structural phase transition in Na_{1.32}Mn[Fe(CN)₆]_{0.83}·3.6H₂O” [J. Phys. Soc. Jpn. 80, 074608 (2011)]. *J. Phys. Soc. Japan* **85**, 038001 (2016).
- Niwa, H., Kobayashi, W., Shibata, T., Nitani, H. & Moritomo, Y. Invariant nature of substituted element in metal-hexacyanoferrate. *Sci. Rep.* **7**, 13225 (2017).
- Matsuda, T. & Moritomo, Y. Thin film electrode of Prussian blue analogue for li-ion battery. *Appl. Phys. Express* **4**, 047101 (2011).

5. Moritomo, Y., Takachi, M., Kurihara, Y. & Matsuda, T. Thin film electrodes of Prussian blue analogues with rapid Li⁺ intercalation. *Appl. Phys. Express* **5**, 041801 (2012).
6. Takachi, M., Matsuda, T. & Moritomo, Y. Structural, electronic, and electrochemical properties of Li_xCo[Fe(CN)₆]_{0.90}·2.9H₂O. *Jpn. J. Appl. Phys.* **52**, 044301 (2013).
7. Takachi, M., Matsuda, T. & Moritomo, Y. Cobalt hexacyanoferrate as cathode material for Na + secondary battery. *Appl. Phys. Express* **6**, 025802 (2013).
8. Takachi, M., Matsuda, T. & Moritomo, Y. Redox reactions in Prussian blue analogue films with fast Na + intercalation. *Jpn. J. Appl. Phys.* **52**, 090202 (2013).
9. Yang, D. *et al.* Structure optimization of Prussian blue analogue cathode materials for advanced sodium ion batteries. *Chem. Commun.* **50**, 13377–13380 (2014).
10. Lu, Y., Wang, L., Cheng, J. & Goodenough, J. B. Prussian blue: A new framework of electrode materials for sodium batteries. *Chem. Commun.* **48**, 6544–6546 (2012).
11. Lee, H.-W. *et al.* Manganese hexacyanomanganate open framework as a high-capacity positive electrode material for sodium-ion batteries. *Nat. Commun.* **5**, 5280 (2014).
12. Wang, L. *et al.* Rhombohedral Prussian white as cathode for rechargeable sodium-ion batteries. *J. Am. Chem. Soc.* **137**, 2548–2554 (2015).
13. Yu, S. *et al.* A promising cathode material of sodium iron-nickel hexacyanoferrate for sodium ion batteries. *J. Power Sources* **275**, 45–49 (2015).
14. Pramudita, J. C. *et al.* Sodium uptake in cell construction and subsequent in operando electrode behaviour of Prussian blue analogues, Fe[Fe(CN)₆]_{1-x}·yH₂O and FeCo(CN)₆. *Phys. Chem. Chem. Phys.* **16**, 24178–24187 (2014).
15. Zhu, K., Li, Z., Jin, T. & Jiao, L. Low defects potassium cobalt hexacyanoferrate as a superior cathode for aqueous potassium ion batteries. *J. Mater. Chem. A* **8**, 21103–21109 (2020).
16. Bak, S. M., Shadik, Z., Lin, R., Yu, X. & Yang, X. Q. In situ/operando synchrotron-based X-ray techniques for lithium-ion battery research. *NPG Asia Mater.* **10**, 563–580 (2018).
17. Yue, J. L. *et al.* O3-type layered transition metal oxide Na(NiCoFeTi)_{1/4}O₂ as a high rate and long cycle life cathode material for sodium ion batteries. *J. Mater. Chem. A* **3**, 23261–23267 (2015).
18. Karan, N. K. *et al.* Operando structural characterization of the lithium-substituted layered sodium-ion cathode material P2-Na_{0.85}Li_{0.17}Ni_{0.21}Mn_{0.64}O₂ by X-ray absorption spectroscopy. *J. Electrochem. Soc.* **161**, A1107–A1115 (2014).
19. Kubota, K. *et al.* New insight into structural evolution in layered NaCrO₂ during electrochemical sodium extraction. *J. Phys. Chem. C* **119**, 166–175 (2015).
20. Huang, W. *et al.* Detailed investigation of Na_{2.24}FePO₄CO₃ as a cathode material for Na-ion batteries. *Sci. Rep.* **4**, 4188 (2015).
21. Mullaliu, A. *et al.* Copper electroactivity in Prussian blue-based cathode disclosed by operando XAS. *J. Phys. Chem. C* **122**, 15868–15877 (2018).
22. Reguera, E., Bertrán, J. F., Díaz, C., Blanco, J. & Rondón, S. Mössbauer and infrared spectroscopic studies of novel mixed valence states in cobaltous ferrocyanides and ferricyanides. *Hyperfine Interact.* **53**, 391–395 (1990).
23. Sato, O., Einaga, Y., Iyoda, T., Fujishima, A. & Hashimoto, K. Cation-driven electron transfer involving a spin transition at room temperature in a cobalt iron cyanide thin film. *J. Phys. Chem. B* **101**, 3903–3905 (1997).
24. Nakada, F., Kamioka, H., Moritomo, Y., Kim, J. E. & Takata, M. Electronic phase diagram of valence-controlled cyanide: Na_{0.84-δ}Co[Fe(CN)₆]_{0.713}·3.8H₂O (0 ≤ δ ≤ 0.61). *Phys. Rev. B* **77**, 224436 (2008).
25. Bleuzen, A. *et al.* Photoinduced ferrimagnetic systems in Prussian blue analogues C¹_xCo₄[Fe(CN)₆]_y (C¹ = alkali cation). 1. Conditions to observe the phenomenon. *J. Am. Chem. Soc.* **122**, 6648–6652 (2000).
26. Lezna, R. O., Romagnoli, R., De Tacconi, N. R. & Rajeshwar, K. Cobalt hexacyanoferrate: Compound stoichiometry, infrared spectroelectrochemistry, and photoinduced electron transfer. *J. Phys. Chem. B* **106**, 3612–3621 (2002).
27. Martínez-García, R. *et al.* Heat-induced charge transfer in cobalt iron cyanide. *J. Phys. Chem. Solids* **67**, 2289–2299 (2006).
28. Risset, O. N., Knowles, E. S., Ma, S., Meisel, M. W. & Talham, D. R. Rb₃M_x[Fe(CN)₆]₁ (M = Co, Ni) Prussian blue analogue hollow nanocubes: A new example of a multilevel pore system. *Chem. Mater.* **25**, 42–47 (2013).
29. Goberna-Ferrón, S., Hernández, W. Y., Rodríguez-García, B. & Galán-Mascarós, J. R. Light-driven water oxidation with metal hexacyanomethylate heterogeneous catalysts. *ACS Catal.* **4**, 1637–1641 (2014).
30. De Tacconi, N. R., Rajeshwar, K. & Lezna, R. O. Metal hexacyanoferrates: Electrochemistry, in situ characterization, and applications. *Chem. Mater.* **15**, 3046–3062 (2003).
31. Zheng, F., Zhu, D., Shi, X. & Chen, Q. Metal-organic framework-derived porous Mn_{1.8}Fe_{1.2}O₄ nanocubes with an interconnected channel structure as high-performance anodes for lithium ion batteries. *J. Mater. Chem. A* **3**, 2815–2824 (2015).
32. Moriya, T., Shibata, T., Fukuzumi, Y., Niwa, H. & Moritomo, Y. Persistence and amalgamation types of CN stretching mode in oxidation process of Prussian blue analogues. *J. Phys. Soc. Jpn.* **89**, 064708 (2020).
33. Kurihara, Y. *et al.* Electronic structure of hole-doped transition metal cyanides. *J. Phys. Soc. Jpn.* **79**, 044710 (2010).
34. Verdager, M. & Girolami, G. S.: Magnetism. in *Molecules and Materials V* (eds. J. S. Millar & M. Drillon), Chap. 9, 283 (Wiley-VCH, Weinheim, 2005).
35. Shibata, T., Iwaizumi, H., Fukuzumi, Y. & Moritomo, Y. Energy harvesting thermocell with use of phase transition. *Sci. Rep.* **10**, 1813 (2020).
36. Igarashi, K., Nakada, F. & Moritomo, Y. Electronic structure of hole-doped Co-Fe cyanides: < Na_{1.60-δ}Co[Fe(CN)₆]_{0.90}·2.9H₂O (0.0 ≤ δ ≤ 0.85). *Phys. Rev. B* **78**, 235106 (2008).
37. Takahara, I., Shibata, T., Fukuzumi, Y. & Moritomo, Y. Improved thermal cyclability of tertiary battery made of prussian blue analogues. *ChemistrySelect* **4**, 8558–8563 (2019).

Acknowledgments

This work was supported by JSPS KAKENHI (Grant Number JP17H0113).

Author contributions

H.N. provided analyzed experimental data, prepared all table and figures and wrote the manuscript. T.M. performed sample preparations, characterizations, and IR measurements. T.S. provided advice on sample preparations. Y.F. provided advice on in situ cell. Y.M. planned the research and wrote the manuscript. All authors read and approved the manuscript.

Competing interests

The authors declare no competing interests.

Additional information

Supplementary Information The online version contains supplementary material available at <https://doi.org/10.1038/s41598-021-83699-8>.

Correspondence and requests for materials should be addressed to H.N. or Y.M.

Reprints and permissions information is available at www.nature.com/reprints.

Publisher's note Springer Nature remains neutral with regard to jurisdictional claims in published maps and institutional affiliations.



Open Access This article is licensed under a Creative Commons Attribution 4.0 International License, which permits use, sharing, adaptation, distribution and reproduction in any medium or format, as long as you give appropriate credit to the original author(s) and the source, provide a link to the Creative Commons licence, and indicate if changes were made. The images or other third party material in this article are included in the article's Creative Commons licence, unless indicated otherwise in a credit line to the material. If material is not included in the article's Creative Commons licence and your intended use is not permitted by statutory regulation or exceeds the permitted use, you will need to obtain permission directly from the copyright holder. To view a copy of this licence, visit <http://creativecommons.org/licenses/by/4.0/>.

© The Author(s) 2021